Supplementary materials for

"Nanocrystals generated under tensile stress in metallic glasses with phase selectivity"

Yancong Feng,[ab#] Wei-Bing Liao,[ac#] Jiaxin Zheng,[a] Lin-Wang Wang,[d*] Yong Zhang,[e*] Jianfei Sun[f] and Feng Pan[a*]

[a] School of Advanced Materials, Peking University Shenzhen Graduate School, Shenzhen 518055, China

[b] South China Academy of Advanced Optoelectronics, South China Normal University, Guangzhou 510006, China

[c] College of Physics and Energy, Shenzhen University, Shenzhen 518060, China

[d] Materials Science Division, Lawrence Berkeley National Laboratory, Berkeley, California 94720, United States

[e] State Key Laboratory for Advanced Metals and Materials, University of Science and Technology Beijing, Beijing 100083, China

[f] School of Materials Science and Engineering, Harbin Institute of Technology, Harbin 150001, China

* Corresponding author.

E-mail: lwwang@lbl.gov (Lin-Wang Wang); drzhangy@ustb.edu.cn (Yong Zhang);

panfeng@pkusz.edu.cn (Feng Pan).

[#]These authors contributed equally.

Supplementary Information

SI.1: Preparing the $Cu_{50}Zr_{50}$ alloy rod with a diameter of 5 mm and characterizing the phase microstructures.

SI.2: Preparation, tension and characterization of metallic glassy wires.

SI.3: Comparison of attractive basins of the B2 and B19’ structure under stress.

SI.4: Thermodynamic analysis of the phase transition from B19' to B2 under uniaxial strain.

SI.5: Dynamic analysis of the phase transition between B2 and B19' under uniaxial strain.

SI.1: Preparing the $Cu_{50}Zr_{50}$ alloy rod with a diameter of 5 mm and characterizing the phase microstructures.

Alloy ingots with a nominal composition of $Cu_{50}Zr_{50}$ (at. %) were prepared by arc-melting a mixture of elements with a purity level of ＞99.9% in a Ti-gettered high purity argon atmosphere. Repeated melting was carried out at least five times to improve the chemical homogeneity of the alloy. The molten alloy was drop-cast into a 5 mm diameter copper mold under argon atmosphere. Fig. S1 shows the selected area electronic diffraction (SAED) patterns of the rod with a diameter of 5 mm are very complex, indicating that multi phases coexist in the alloy.

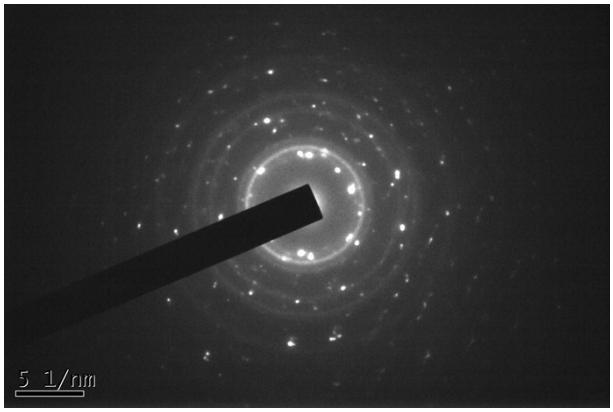

Fig. S1. The selected area electron diffraction patterns of the cast $Cu_{50}Zr_{50}$ alloy rod with a diameter of 5 mm.

Fig. S2 shows the snapshots of primitive cells of (a) B2 (Pm–3m) and (b) B19' ($P2_1/m$) structures. The lattice parameters of cubic B2 structure are: a=b=c=3.262 Å. The lattice parameters of monoclinic B19’ structure are: a=3.301, b=4.138, c=5.273 and β=104.7°. The data of lattice parameters are derived from the ICDD.

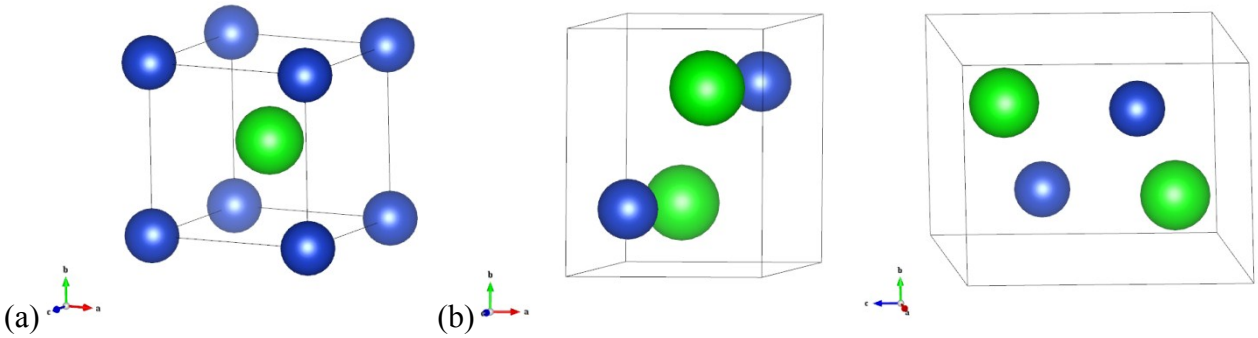

Fig. S2. Snapshots of primitive cells of (a) B2 and (b) B19' structures.

Table S1. Energy of B2 and B19' phase structure.

Phase	Energy (eV atom^{-1})	
	This work	Ref. [1]
B2	-6.2537	-6.2051
B19'	-6.2754	-6.2192

SI.2: Preparation, tension and characterization of metallic glassy wires.

Section 2.1. Preparing the metallic glassy wires by the melt-extracted method and characterizing the microstructures.

Fig. S3(a) is a schematic showing how the micron-sized metallic glassy wires were prepared using a melt-extraction method.). The edge angle of the Cu wheel (diameter about 200 mm) was fixed at 60°. The circumferential velocity V_w of the Cu wheel was 30 ms^{-1}. In the apparatus, the position of the cylindrical rods by induction melting could be controlled. The molten mother alloy was extracted by moving up the melt cylindrical rods under a high purity argon atmosphere, and forming a fine, rapidly cooled circular fiber with a high surface-to-volume ratio [2]. The surface morphologies and actual fiber diameters were examined in a Zeiss SUPRA 55 scanning electron microscope (SEM). Resulting free-standing and flexible microwires with a diameter of 50 μm and 300 mm in length are shown in Fig. S3(b). The magnified microscopic image shows that the microwires are axially and radially uniform with a smooth surface.

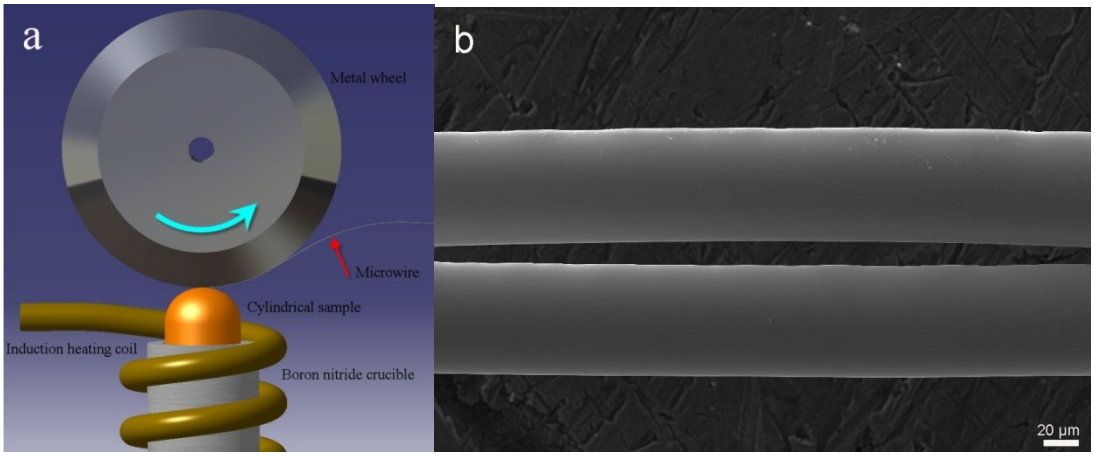

Fig. S3. Samples preparation and the surface characterization. (a) Schematic illustration of a MEM used in the present study. (b) SEM micrographs of the CuZr MGWs.

Section 2.2. Preparing the TEM sample of the micron-sized wires.

The microstructures of the samples were examined by HRTEM using a TECNAI-F30 instrument operated at 300 kV. Before the wire sample was investigated by HRTEM, it was pasted on a copper ring and treated by ion milling using the Gatan Model 691 precision ion polishing system. In order to avoid the crystallization induced by the ion beams, liquid nitrogen cooling was employed during the experiments.

Fig. S4(a) shows the surface X-ray diffraction pattern of the wire samples. The scanning rate is 0.00185 degree/s. Only a broad diffuse peak without any evidence of crystalline phases is seen for all the samples, indicating that these wires are fully amorphous. The crystallization enthalpy of the prepared wires showed in Fig. S4(b) was around 100 J/g, which also confirmed the amorphous structures. The wire samples exhibited the similar thermal behavior with no obvious sign of glass transition process. The weak glass transition event for the metallic glass wires is probably due to the facts that the significant structure relaxation released amount of enthalpy before glass transition and it occurred too closely with the crystallization and was covered by the strong signal from the later reaction.

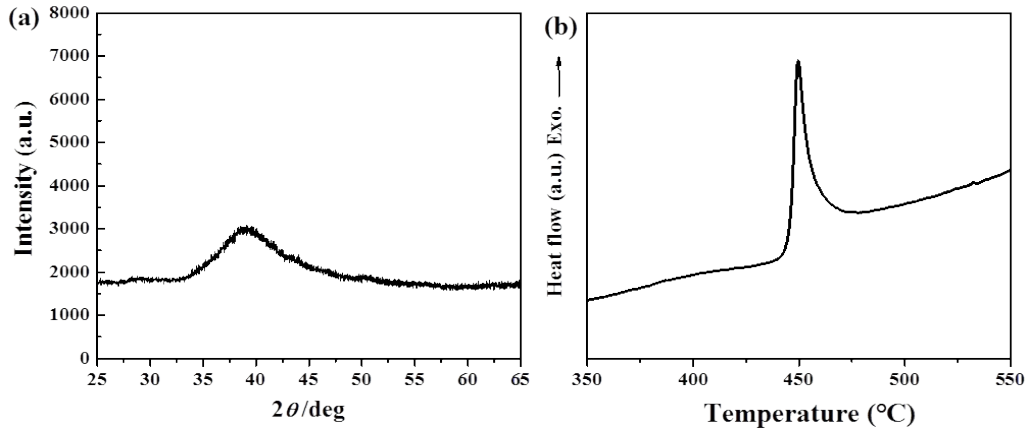

Fig. S4. (a) X-ray diffraction (XRD) pattern and (b) differential scanning calorimetry (DSC) curve of the metallic glassy wires after cooling.

Section 2.3. Tensile test analysis of the metallic glassy wires.

Tension experiments were conducted on an Instron 5848 micro tester with a gauge length of 20 mm and a strain rate of 8.33×10^{-5} s^{-1} at room temperature. The test wires were bonded to a specially designed paper frame with a rhombic hole at the center by the epoxy adhesive, as shown in Fig. S5. When the testing sample was fixed on the crosshead, the paper frame was cutoff through the middle. As loading on the sample, initially the sample deformed elastically, and not until the strain reaching 1.20 %, unloading was employed on the sample.

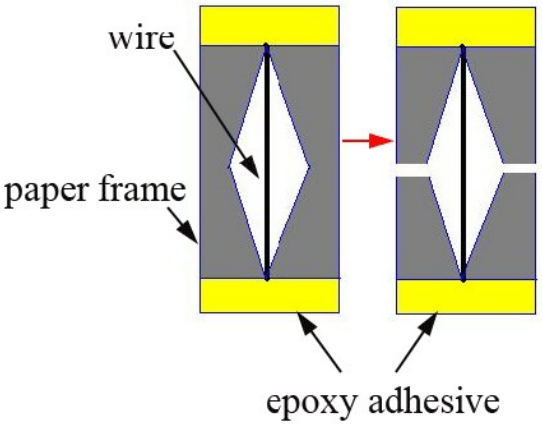

Fig. S5. Schematic illustration of the wire tensile testing assembly. The wire was adhered to the paper frame with a rhombic hole at the center by epoxy adhesive.

SI.3: Comparison of attractive basins of the B2 and B19' structure under stress.

For the comparison of attractive basins and the thermodynamic analysis, density functional theory (DFT) calculations were performed using the projector-augmented wave methods implemented in the Vienna ab initio simulation package (VASP). The Perdew-Burke-Ernzerhof (PBE) form of the generalized gradient approximation (GGA) was selected as the exchange-correlation potential. The plane wave energy cutoff was set to 520 eV. The maximum residual force was less than 0.02 eV/Å. The k-point mesh was set to be $3\times3\times3$. The B2 ($3\times2\sqrt{2}\times2\sqrt{2}$ unit cells) and B19' ($3\times2\times2$ unit cells) supercells were built, shown in Fig. S6.

During the transformation, the lattice is transformed gradually and uniformly in 10 steps, and then relaxed. The B19′ structure can be transformed to the B2-like structure; however, the B2supercell keeps the same structure after lattice transition and relaxation, shown in Fig. S7. Then, the evolution of B19′ to B2-like structure is focused. Fig. S8 shows that, before step 6, the supercell retunes to the B19′ structure. The step 6~7 are the transition states. After step 8, the supercell transforms to be B2-likestructure.

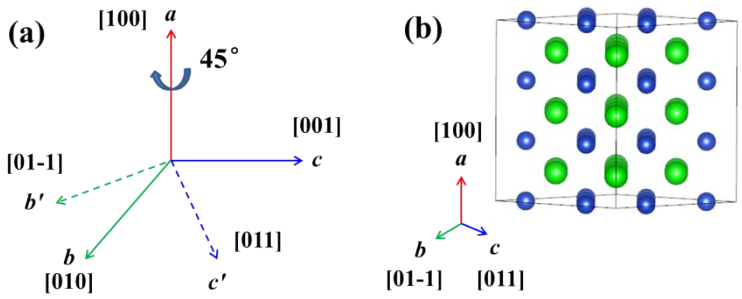

Fig. S6. Schematic representation of B2($3\times2\sqrt{2}\times2\sqrt{2}$ unit cells) structure. (a) The new coordinate system is transformed from the body-cubic coordinate system by rotating 45° deasil around the *a*-axis. (b) Snapshot of the B2($3\times2\sqrt{2}\times2\sqrt{2}$ unit cells) structure.

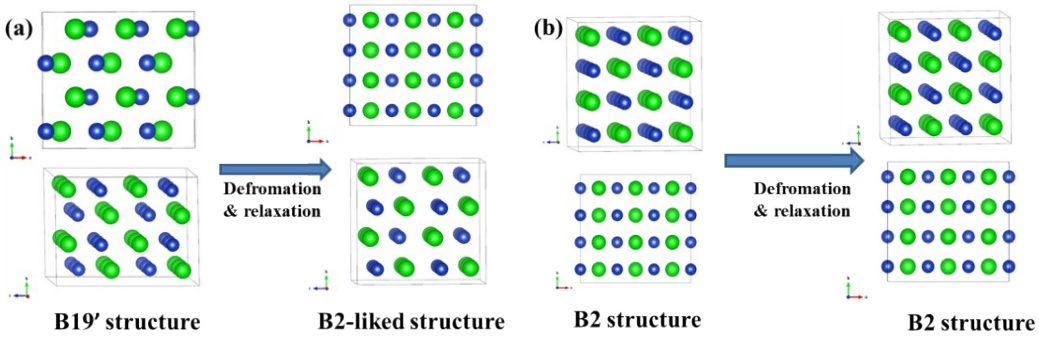

Fig. S7. Snapshots of CuZr alloy before and after deformation. (a) B19' lattice was transformed to B2 one, and then relaxed to the B2-like structure. (b) B2 lattice was transformed to B19' one, and ultimately retuned to the B2 structure.

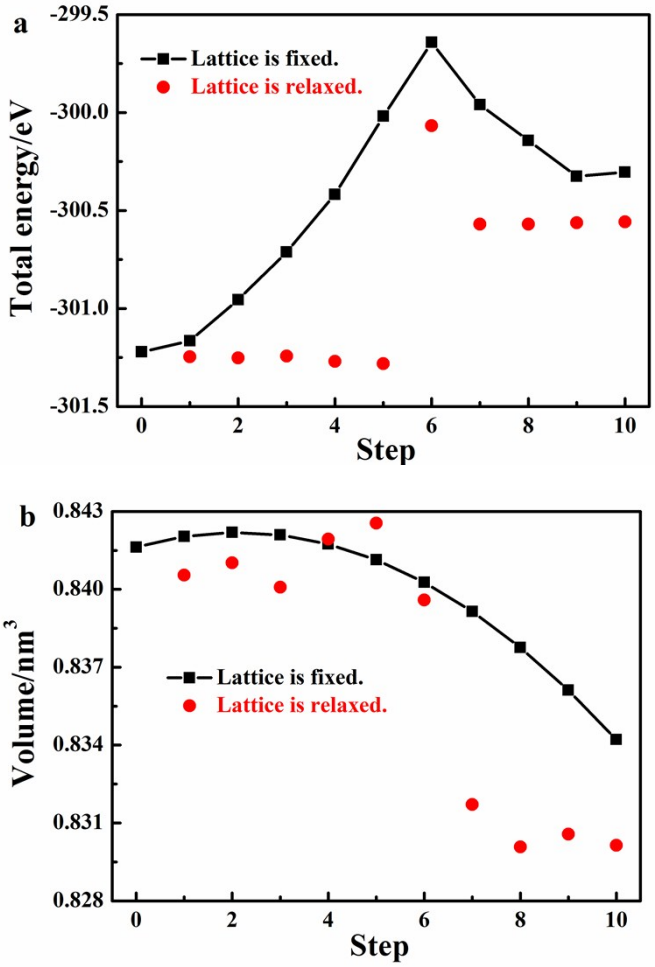

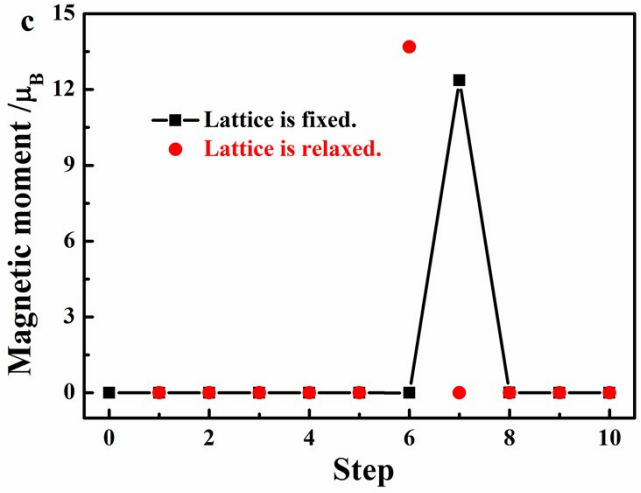

Fig. S8. Evolutions of (a) energies, (b) volumes and (c) magnetic moments of the system during the transformation from B19' to B2 lattice. The black line denotes that the lattice parameters are fixed. Each image generated during the transformation is relaxed, and the corresponded physical quantities are expressed by the red dots.

To judge whether the phase transition occurs, the structure is described by the Voronoi polyhedron, which is the best method for the analysis of topological structure. The Voronoi Index [3] $<n_3, n_4, n_5, n_6>$ can effectively determine the type of polyhedron, where n_i denotes the number of i-edged faces of polyhedron centered around the certain atom.

SI.4: Thermodynamic analysis of the phase transition from B19' to B2 under uniaxial strain.

The thermodynamic phase transitions under hydrostatic pressure are well studied [4,5]. Under pressure P, the thermodynamic property which determines the crystal phase is not the internal energy E, but the Gibbs free energy $G = E + PV - TS$. The ab initio calculations are done at 0 K, and thus the enthalpy $H = E + PV$ determines the crystal phase. The situation for uniaxial stress is more complicated. Under elastic stress, we can assume that there is no crystal orientation rotation, but only small deformations. Thus, we have applied uniaxial tension in the three crystal lattice directions of the crystal phase B19'. Under each stress ε, we find a mostly likely path of crystal cell change, gradually from B19' to B2, which can both release the energy but also have a smooth path. Thus the difference of the enthalpy ΔH between the B19' and B2 phases under this uniaxial stress will equal to their energy difference $E_2 - E_1$ under this stress, and the work W to change the cell shape from B19' to B2. In other word:

$$\Delta H = E_2 - E_1 + W \tag{1}$$

where E_1 and E_2 are the internal energies of phase 1 and phase 2 under stress ε (i.e., both deformed B19' and B2 cells under ε), and work W if the cell is changed from phase 1 to phase 2, which can be written as (see Ref. [6])

$$W = P_X \int_1^2 l_y l_z dl_x + P_Y \int_1^2 l_x l_z dl_y + P_Z \int_1^2 l_x l_y dl_z \tag{2}$$

where l_x, l_y and l_z are the x, y, z direction lattice length, and P_X, P_Y, P_Z are uniaxial pressure (stress) in the x, y, z directions. Under uniaxial tension (Z-direction), P_X and P_Y are zero. Therefore, the principle for the phase transition can be written as

$$\Delta H = E_2 - E_1 + P_Z \int_1^2 l_x l_y dl_z \le 0 \tag{3}$$

Fig. S9 shows the snapshots of B19' and B2 structures at phase transition, e.g. $\Delta H = 0$. The

coordinates and the internal forces of atoms at the first layer are calculated in Table S2. The results show that the average internal forces of atoms of B19' structure in the Z-direction are much higher than others, indicating the anisotropy. Combined the coordinates and the forces of atoms, the moving directions of the atoms at phase transition can be confirmed, shown in Fig. S9.

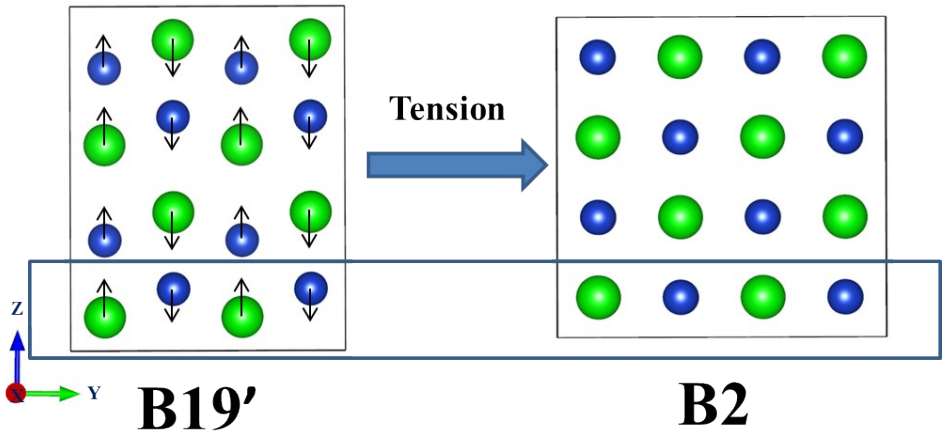

Fig. S9. Snapshots of B19' and B2 structures at $\Delta H = 0$, where the uniaxial tension was added in the Y-direction. The arrows show the moving directions of the atoms if the phase transition occurs. The atoms in the first layer are shown in the frame.

Table S2. Average coordinates and the internal forces of atoms at the phase transition from B19' to B2.

Phase	Atom	Force *10^5/eV Å^{-1}			Coordinate
		X	Y	Z	Z
B19'	Zr	-6.283	-0.1500	1279	0.0977
	Cu	-421.5	-0.2000	-1389	0.1795
B2	Zr	-0.1000	106.8	59.12	0.125
	Cu	-0.1000	410.8	-167.2	0.125

SI.5: Dynamic analysis of the phase transition between B2 and B19' under uniaxial strain.

In a dynamic view, molecular dynamics simulations were adopted to study the phase transition, using the code LAMMPS. The embedded-atom method (EAM) potentials were used [7]. The NPT ensemble is employed, and the temperature is fixed at $T = 300\,\mathrm{K}$ by using the Nose–Hoover thermostat. Periodic boundary conditions are adopted in all three directions. The velocity–Verlet algorithm is applied to integrate the equations of motion with a time step 1 fs.

The evolutions of structures and the stress–strain behaviors during the uniaxial tensile were investigated by the means of molecular dynamics simulations, shown in Fig. 5 in the manuscript. The B2 and B19' primitive cells were based on the results of ab initio calculations. B2 ($15\times10\sqrt{2}\times10\sqrt{2}$ unit cells) and B19' ($15\times10\times10$ unit cells) supercells were built. The systems were stretched along the Y-direction, and the strain rates were $5\times10^{8}\ s^{-1}$. The average stress σ in the Y-direction is expressed by [8] $\sigma = (1+\mu)(P_Y - P)$, where $P = \sum_i P_i / 3$ is the hydrostatic pressure, and $\mu = 0.415$ according to the literature [9]. The atom number must be large enough for the study of deformation behavior in molecular dynamics simulations. The 6,000-atoms (Fig. 5(a,c) and 48,000-atoms system (Fig. S10(a,b) were compared. Comparing Fig. 5 and Fig. S10, it was found that the stress-strain behavior was almost the same as the 6,000-atoms systems, but the evolution of structures is much clearer for the 6,000-atoms system, which has a size closed to the nanocrystals observed in the experiments. As the results of the two systems are almost the same, in order to clearly observe the evolution of the structures, we put the smaller system (6,000-atoms) in the manuscript.

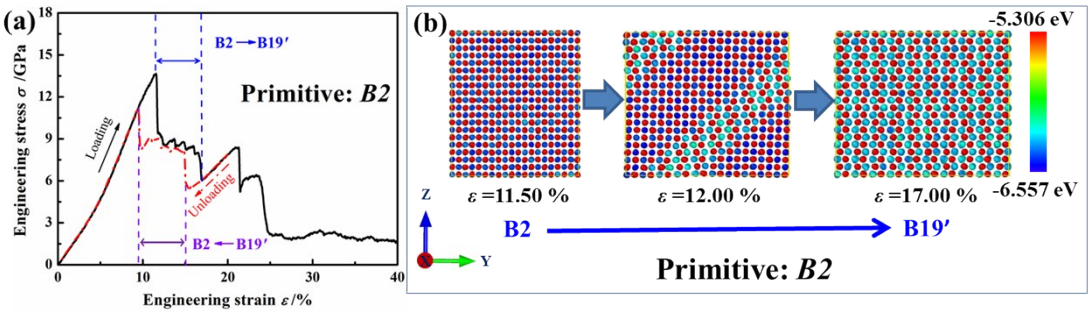

Fig. 5. (a) Stress-strain behaviors and (b) the evolutions of structures for the 6,000-atoms system during the uniaxial tensile.

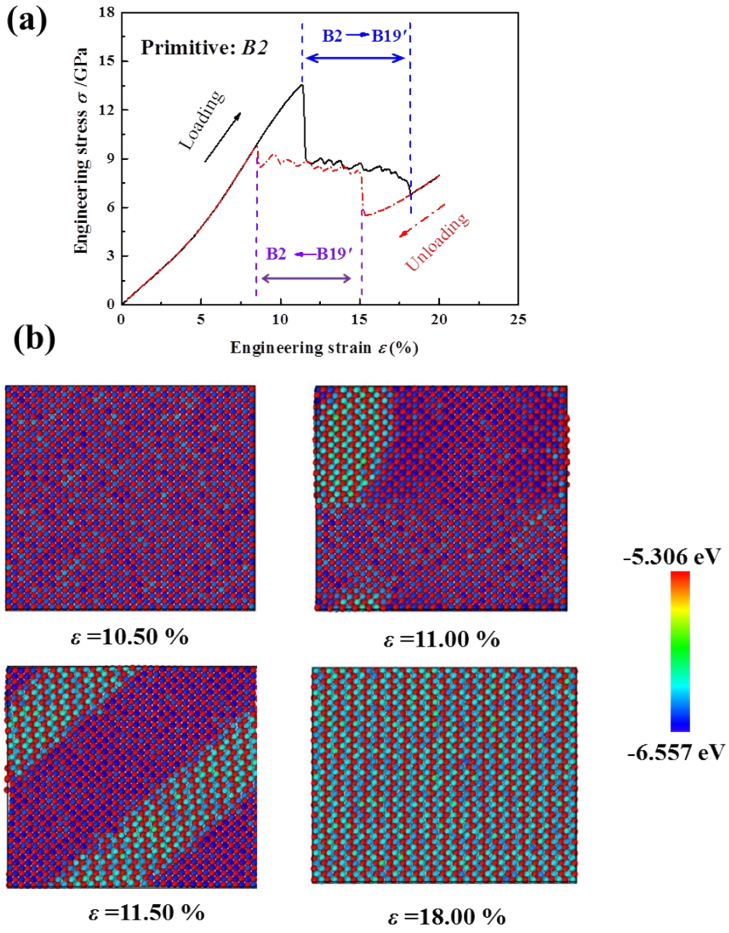

Fig. S10. (a) Stress-strain behaviors and (b) the evolutions of structures for the 6,000-atoms system during the uniaxial tensile.

The stress-strain curve shown in Fig. 5b in the manuscript presents that B19' phase starts to transfer

to the B2 one at engineering strain ε = 4.00 %. The length of B19' supercell in Y-direction (tensile direction) at ε = 4.00 % is about 4.4 nm, whereas the length of B2 one in the same direction without any stress is 4.6 nm. It means that the stress added on the supercell change from tension to compression during the phase transition. In the MD simulations of this work, the positive stress represents the tension whereas the negative one denotes the compression. Once the engineering strain ε reaches to 9.05%, the length of B19' supercell in tensile direction is about 4.6 nm, equaling to the length of B2 one without any stress. Hence, the engineering stress rises from negative to 0, as shown in Fig. 5b in the manuscript.

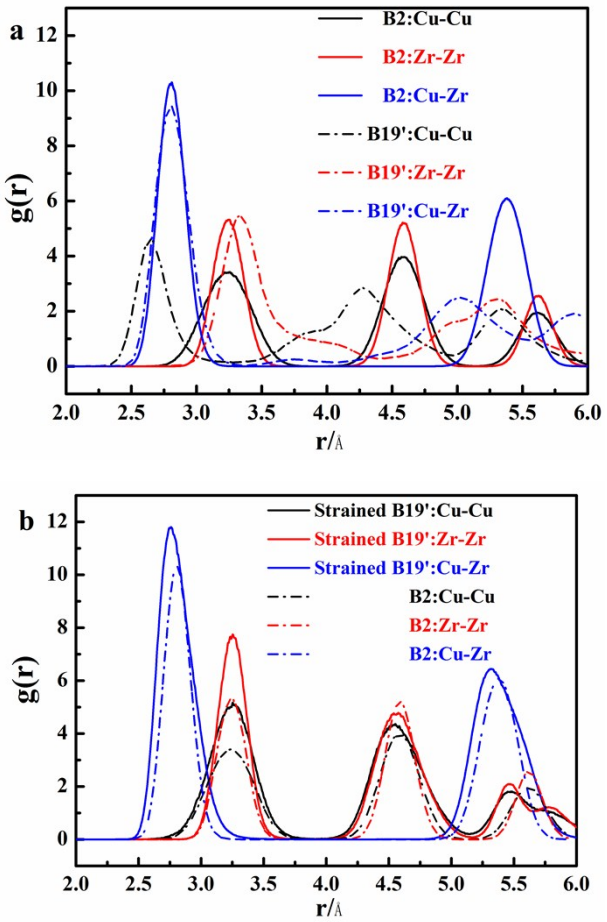

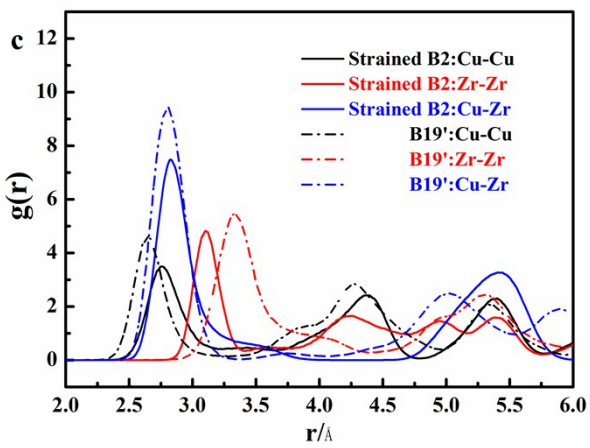

Fig. S11. Radial distribution functions at 300 K. (a) The B2 ($15\times10\sqrt{2}\times10\sqrt{2}$ unit cells) and B19' ($15\times10\times10$ unit cells) crystals are unloaded. (b) Comparison of unstrained B2 structure and strained B19' one, where the strain $\varepsilon = 4.50\ \%$. (c) Comparison of unstrained B19' structure and strained B2 one, where the strain $\varepsilon = 17.00\ \%$.

Supplementary Information References

[1] S.H. Zhou and R.E. Napolitano, Scripta Mater. 59 (2008) 1143.

[2] W. Liao, J. Hu, and Y. Zhang, Intermetallics 20 (2012) 82.

[3] J.L. Finney, Proc. R. Soc. 319 (1970) 479.

[4] M.T. Yin and M.L. Cohen, Phys. Rev. Lett. 50 (1983) 2006.

[5] R.J. Needs and R.M. Martin, Phys. Rev. B 30 (1984) 5390.

[6] C. Cheng, W.H. Huang, and H.J. Li, Phys. Rev. B 63 (2001) 153202.

[7] M.I. Mendelev, M.J. Kramer, R.T. Ott, D.J. Sordelet, D. Yagodin, and P. Popel, Philos. Mag. 89 (2009) 967.

[8] D.R. Rottach, J.G. Curro, G.S.G. And, and A.P. Thompson, Macromolecules 37 (2004) 5468.

[9] M.I. Mendelev, D.K. Rehbein, R.T. Ott, M.J. Kramer, and D.J. Sordelet, J. Appl. Phys. 102 (2007) 093518.